Title

Micro-cantilever beam experiments and modeling in porous polycrystalline UO2

Authors

Gong, Bowen

Frazer, David

Shaffer, Benjamin

et al.

Publication Date

2021-12-01

DOI

10.1016/j.jnucmat.2021.153210

Micro-cantilever Beam Experiments and Modeling in Porous Polycrystalline UO_2

Bowen Gong[1], David Frazer[2,3,*], Benjamin Shaffer[1], Harn Chyi Lim[1], Peter Hosemann[2,4], Pedro Peralta[1]

[1]School for Engineering of Matter, Transport, and Energy, Arizona State University, Tempe, AZ 85287, United States
[2]Nuclear Engineering Department, University of California, Berkeley, 4153 Etcheverry Hall Berkeley, CA
[3] Advanced Characterization and PIE, Idaho National Laboratory, 2525 Fremont Ave, Idaho Falls, ID USA
[4] Material Science Division, Lawrence Berkeley National Laboratory, Berkeley, CA
*David.frazer@inl.gov

Keywords: oxide nuclear fuel, microscale mechanical testing, effect of porosity, finite element modeling

Abstract

Understanding the impact of microstructure on the thermo-mechanical behavior of oxide nuclear fuels is vital to predict their performance through multiscale models. Evaluating the mechanical properties at the sub-grain length scale is key to developing these multiscale models. In this work, 3D finite element (FE) models were constructed to simulate the micrometer-scale bending of micro-cantilever beams fabricated using porous polycrystalline uranium dioxide (UO_2) and tested at room temperature. The results showed that the porosity and elastic anisotropy of individual grains can play a significant role in determining the mechanical properties of the material. Specifically, the porosity had a non-negligible effect, given that the pore size was of the same order of magnitude as the dimensions of the micro-beams. Correlations between load-deflection data, pore location, and elastic properties (effective Young's modulus) were investigated using UO_2 micro-beam FE models, where pore clusters were included and placed at different locations along the length of the beam. Results indicated that the presence of pore clusters near the substrate, i.e., the clamp of the micro-cantilever beam, has the strongest effect on the load-deflection behavior, with the porosity leading to a reduction of stiffness that is the largest for any locations of the pore clusters. Furthermore, it was also found that pore clusters located towards the middle of the span and close to the end of the beam have a comparatively small effect on the load-deflection behavior, thus it is concluded that accurate estimates of Young's modulus can be obtained from micro-cantilever experiments after accounting for porosity on the one third of the beam length close to the clamp. This, in turn, provides an avenue to improve microscale experiments and their analysis in porous, anisotropic elastic materials.

1. Introduction

Understanding the thermo-mechanical behavior of oxide fuels is extremely important to comprehend and predict the overall fuel performance. Careful experimental measurements of mechanical properties are key for the validation of robust fuel performance codes, which able to predict material behavior [1, 2]. In UO_2, the local thermo-mechanical response depends strongly on the crystal orientation of individual grains and the presence of pores or pore clusters, both of which impact the properties of the bulk material. The porosity in the nuclear fuel is important as it can affect mechanical properties such as Young's modulus [3, 4], strength [5], hardness and

fracture toughness [4, 6], as well as thermal conductivity [7] of the fuel at the macroscale, even though the pore size and spacing are commensurate with the fuel's microstructure. Therefore, careful quantification of the mechanical response at the sub-grain level will be key to validate advanced fuel performance codes with multiscale predictive capabilities. Macroscale testing of single crystals would be ideal for measuring mechanical properties at the microscale but growing large crystals of UO_2 is difficult and costly. Therefore, micro-scale testing can be used to measure the elastic, plastic, and fracture behavior of nuclear fuels within individual grains as an alternative and practical approach. Furthermore, developing a framework to perform such tests would enable similar tests after irradiation of UO_2 and other highly activated materials in the future [8-12]. Micro-scale mechanical testing is a growing field for the study of the mechanical properties of nuclear fuels and needs to be developed on fresh fuels [13-19] prior to their more widespread use on irradiated fuels [20-23].

Porosity is found to be important for the performance of oxide nuclear fuels and has a significant impact on the mechanical properties of UO_2 [24, 25]. Hence, it is crucial to take it into account when conducting experiments and modeling simulations to explore its thermomechanical behavior. Furthermore, since the size and distribution of the pores are of a similar length scale as the geometry of the testing specimens, there may be more variability in the results from micro-scale testing comparing to the bulk testing. Thus, understanding the role of pores in the micro-cantilever testing is critical and essential. When the sample is smaller than the representative volume element (RVE), elastic moduli can differ significantly from average values [26, 27], which must be taken into account for the correct interpretation of experimental results. In addition, the elastic anisotropy in UO_2 can affect the results, especially at larger grain sizes. This leads us to explore the effects of grain orientation in this study.

In the present study, the aim is to study the relationships among pore and grain orientation distributions along the length of UO_2 micro-cantilever beams and their effects on the load-deflection behavior of the microcantilever beams. Then, the value of Young's modulus extracted from these experiments is used to deduce experimental and data analysis procedures to measure values of mechanical properties in UO_2 at the sub-grain scale.

2. Experimental Methods

A UO_2 sample with an average grain size of around 8-10 μm and a porosity of 5% was used in this work. The sample was provided by Los Alamos National Laboratory (LANL). The green pellet was compacted at 160 MPa and sintered at 1680 °C using a heating rate of 20 °C/min with no dwell time. The environment was ultra-high purity Argon with an O_2 trap. This pellet was then heat treated at Arizona State University at 1200 °C in an environment with a partial oxygen pressure of $7x10^{-7}$ atmosphere. The heat treatment was 5 hours long, and the sample was kept in the furnace for another 2.5 hours at 1200 °C under Argon + 4% hydrogen atmosphere to reduce to an oxygen to metal ratio (O/M) of ~ 2. Samples were polished using 9, 6, 3, and 1 μm diamond paste and finished with 0.05 μm colloidal silica.

A FEI Quanta dual beam (SEM/FIB) system was used to manufacture the micro-cantilevers. The microcantilever geometry chosen for this study is the one proposed by Di Maio and Roberts [28]. This geometry is more difficult to fabricate and analyze but has the advantage that it can be

manufactured anywhere on the sample. This allows for the potential to place the cantilever in a specific orientation or locating grains large enough to contain the entire micro-cantilever.

A typical manufacturing procedure included the following steps: First of all, three trenches were cut 20-30 μm wide and 10 μm deep with a 7-15 nA at 30 keV Ga ion beam current on three sides to shape the microcantilever. These trenches formed a U-shaped trench cut that defined the rough geometry of the beam. Secondly, the geometry was refined using a 1-3 nA at 30 keV beam current. The samples were then tilted to 45° along the length axis to shape the beam, and the base of the cantilever was undercut from both sides using a 1-3 nA beam current. Next, the undercut at the 45º angle produced the additional triangle on the bottom of the cantilever. After the undercutting and cleanup of the micro-cantilever, the sides of the beam were cut to produce a shape as symmetric as possible. The dimension of the cantilevers manufactured was between 20-30 μm long, 3-6 μm wide, and 2-5 μm in height. The shape and geometry of a representative micro-cantilever beam is shown in Figure 1.

Load-deflection curves for these micro-cantilever beams were obtained using both an ex-situ MicroMaterials Platform 3 indenter and an in-situ Hysitron PI-85 system. Four of the microcantilevers were tested with the MicroMaterials indenter, while one microcantilever was tested in-situ utilizing the Hysitron PI-85 system. The micro-cantilevers tested in the MicroMaterials system were loaded in the displacement-control mode at a constant displacement rate of 10 nm/s until fracture using a dull diamond Berkovich tip. The micro-cantilever beam tested in-situ was loaded at a rate of 10 nm/s with a flat punch tip but not loaded until fracture and sectioned for 3D electron backscatter diffraction (EBSD) microstructural analysis. A representative load-displacement curve was shown in Figure 2a, along with the nanoindenter and the microcantilever tested in-situ shown in Figure 2b.

Results were collected from several beams, and the slope of the curves were obtained from their linear portions using the least squares method. This slope was, in turn, used to estimate the value of Young's modulus from a simple beam theory analysis, i.e., where P is the load, E is Young's modulus, I is the moment of inertia, L is the distance between the point of application of the load and the substrate, and δ is the deflection. This approach has been used successfully to evaluate the anisotropy of elastic constants in metallic materials [29, 30] and the Young's modulus for a variety of other materials [16, 29, 31-36].

$$dP/d\delta = \frac{3EI}{L^3} \tag{1}$$

For the ex-situ testing using the MicroMaterials indenter, a scanning feature that allows the topographical mapping of the sample surface with a small load (~2 μN) was utilized. A micro-cantilever beam would be located with the attached optical microscope, and then a scan would be performed over the microcantilever. An image of one of these scans can be seen in Figure 1. As the y and z locations are recorded for each point, it enables using the distance between two points to calculate the lengths needed for equation (1). This allowed for the accurate measurement of the distance between the potential fracture surface and the loading location (L)

for equation (1). In the in-situ case, the distance between the loading location and the potential fracture surface could be measured directly from the image.

Elastic anisotropy in UO_2 makes EBSD necessary to identify the orientation of the grains in the microcantilevers. The EBSD was performed with an Oxford EBSD detector and analyzed with the channel 5 software Tango. The EBSD was performed with 30 keV electrons and a step size of 100 nm. Since EBSD is essentially a surface technique, it is necessary to section the micro-cantilever beam to generate a 3D model of a microcantilever with a detailed inner microstructure. The sectioning of the micro-cantilever beam with EBSD at each step allows for inspecting and analyzing the geometry and location of grains and the pores throughout the micro-cantilever beam. In order to achieve this, a micro-cantilever beam was loaded in-situ in the SEM with the Hysitron PI-85 system and a 5 µm diamond flat punch but not taken to fracture. The FIB was then used to section the micro-cantilever, and EBSD was performed on each section step. The loading curve and the microcantilever during testing can be seen in Figures 2a and 2b. The micro-cantilever beam was sectioned to allow for investigating the internal microstructure. The thickness of each layer obtained from the serial sectioning was respectively 0.71 µm, 1.34 µm, 0.76 µm, 0.52 µm, 0.58 µm, and 1.17 µm. The EBSD was also performed with an Oxford system attached SEM/FIB system at 30 keV with a step size of 50 nm. The microcantilevers that were tested ex-situ in the micromaterials indenter only had their top surface analyzed with EBSD.

3. Modeling Approach

The modeling work was conducted mostly with the finite element (FE) analysis package Abaqus™ and the data visualization software Avizo™. All FE models were created in Abaqus™ using the sample dimensions as measured using SEM. Materials with specific mechanical properties, such as Young's modulus and Poisson's ratio (0.32), were also created and assigned to each model. Meshes were generated either in Abaqus™ for simple models or in HyperMesh™ for more complicated models. The load is applied whether as a point load or as pressure on several elements in the middle of the width, with the distance between the center of the region of these elements to the substrate equals to that of the experiment. The pressure was calculated as the ratio of the load to the area of the region. The substrate of the beams was modeled as a rectangular parallelepiped with dimensions larger than the cross-section of the beam and was constrained with zero displacements on all surfaces except at the top. Models of a non-porous beam with different substrate sizes were run, and the final dimensions chosen for the substrate were such that the boundary conditions on it did not perturb the stress fields significantly at the location where the beam attaches. The results in [8] also show that for aspect ratios, length to width (L/w), larger than 6 the substrate does not play a significant role, so the models in this work use L/w ~ 7 for this reason. An example of a model of the microcantilever can be seen in Figure 3.

For the 3D reconstruction, images of the cross-section along the height of the beam collected using FIB and EBSD with the 3D serial sectioning techniques described above. The beam was sliced and scanned about every 1 µm, and the raw images were obtained. These images were pre-processed first and then imported into Avizo. The pre-processing includes splitting,

cropping, and image size adjusting to make sure the size of the images is the same and can be aligned and imported to Avizo. The importing process involves using the Avizo stacked slices tool, since the thickness of each layer was not identical. In Avizo, each EBSD image was regarded as a slice view for the whole beam and was segmented and labeled with various colors representing different grains, based on the grain boundaries that were shown in the EBSD images. Subsequently, the linear interpolating tool in Avizo was used to generate the intermediate structures between any two slices, which helps to make the boundary between different grains or pores as smooth as possible. The interpolated structure was used to render a 3D volume view of the whole beam. In this way, the 3D representation of the microcantilever beam can be constructed, maintaining all the microstructures of pores and grains.

4. Results and Discussion

Results from several microcantilevers are shown in Table 1. Beams 1-4 were tested ex-situ in the MicroMaterials system, while beam 5 was tested in-situ and sectioned for the purpose of 3D microstructure reconstruction.

Table 1: Geometry and Young's moduli estimated from five micro-bending tests.

Sample #	Tool	Total length (μm)	Loading length (μm)	Width w (μm)	Height b (μm)	Total height H (μm)	L/w	L/H	Slope (μN/nm)	E (GPa)	Fracture load (mN)
Beam 1	MM	21.2	18.90	4.33	2.38	5.13	4.89	4.13	1120	141	1.09
Beam 2	MM	20.4	17.71	3.42	3.50	6.06	5.97	3.37	1680	123	1.37
Beam 3	MM	19.9	16.38	4.30	2.25	5.33	4.63	3.74	1538	93	1.17
Beam 4	MM	20.8	17.00	3.64	2.74	5.54	5.71	3.75	2025	198	1.19
Beam 5	Hysitron	28.5	27.04	3.99	5.27	7.48	7.15	3.81	1915	147	n/a

The table above shows that the elastic modulus results scattered between 93 and 198 GPa and can differ significantly from that of the polycrystalline and fully-dense UO_2, which is approximately 219.6 GPa [37, 38]. Two potential explanations were considered. The first was the elastic anisotropy of the UO_2. It was found using methods described in [39] that the maximum value of equivalent Young's modulus is 334 GPa along <100> directions and the minimum is 164 GPa along the <111> directions, i.e., it can vary by about a factor of 2. Second, the porosity inside the cantilever can contribute to a reduction of the Young's modulus. In order to address the anisotropy of UO_2, EBSD measurements of the cantilevers were made, as shown in Figure 4, which were then used in the subsequent modeling to extract more accurate elastic properties.

4.1 Effect of Elastic Anisotropy in Grains

Since the grain size in this sample was still not large enough to allow micro-cantilever beams to be manufactured into a single grain, they had to be fabricated encompassing several grains instead. The elastic anisotropy in UO_2 implies that the properties of the grain composite can differ from the single-grain property. In this case, effective Young's moduli were used for each grain rather than a full anisotropic calculation. This is based on the work of Armstrong et al [8],

who showed that the equivalent Young's modulus along the axis of microbeams made in single crystals was enough to understand their elastic behavior. The authors showed this for copper, which has a higher elastic anisotropy than UO_2. The use of effective Young's moduli for this study is based on this premise. A calculation of an effective Young's modulus using a simple model is shown in Figure 5. For beams having the bamboo structure as shown in Figure 5, it is possible to find an analytical relationship between Young's modulus of each grain, the length of it, and the distance between each grain and the end of the beam. The resulting expression is shown in Equation (2). It was obtained using analysis from the classical beam theory, i.e., the Euler-Bernoulli approximation, where $\bar{E}$ is the equivalent Young's modulus, L_i is the length from the end of the beam to the beginning of the grain, L_{i-1} is the length from the end of the beam to the end of the grain, L is the total length of the beam and E_i is the Young's modulus of each single grain.

$$\bar{E} = \left(\sum_{1}^{n} \frac{\left(\frac{L_i}{L}\right)^3 - \left(\frac{L_{i-1}}{L}\right)^3}{E_i} \right)^{-1} \tag{2}$$

The first simple case assumes that the beam consists of 2 different grains, with Young's moduli of 164 GPa and 334 GPa, respectively. If these 2 grains have the same length and the grain with larger Young's modulus is close to the substrate, then the effective Young's modulus for the beam would be about 296 GPa, which is just 11% lower than the grain close to the substrate, instead of 50% as one might have first expected. On the other hand, if the Young's modulus of the grain close to the substrate is 164 GPa and the other one is 334 GPa, then the effective Young's modulus is ~175 GPa, which is just 7% above 164 GPa. These results show that the value of Young's modulus for the beam is strongly dominated by the Young's modulus of the grain close to the substrate. This, of course is not surprising since this is the location of the highest stress. Plots of effective Young's modulus versus the length fraction r (the ratio of the length of the grain close to the free end to the whole length of the beam) can be obtained from equation (2) for these two cases, as shown in Figure 6. It can be concluded that the value of effective Young's modulus obtained from bending is dominated by the behavior of about one-half of the beam close to the substrate. Limitations of this approach are the fact that grains actually have to be arranged in a bamboo structure, and secondly, this method can only account for grains that can be detected by EBSD. In addition, anisotropy can only account for part of the reduction in the measured Young's modulus, therefore the porosity must play an important part as well. This is discussed in the next section.

4.2 Effects of the Location of Pores

To better understand the importance of the location of the pores, four FE models of micro-cantilever beams were created using Avizo, based on the geometry of beam 5. The model was divided into three parts with equal lengths, and cavities were then placed into these three parts respectively to mimic the pores. The first model has no pores, the results of which are used as the reference. The second model has pores concentrated in the first section nearest to the substrate, while the third model has pores located in the middle part of the beam, followed by the

fourth model that has pores at the end of the beam. Pores were arranged in the same pattern among all of the models to simplify comparisons and to mimic the presence of pore clusters, which can be found in actual fuel microstructures and might increase variability in the response due to the interaction of individual pores within the cluster because of their close proximity. The overall porosity was kept at 2.5% in all three cases. A point load was applied on the top surface at approximately 22.9 μm from the clamp, following experimental values. The substrate of the beams was modeled as a rectangular parallelepiped with dimensions slightly larger than the cross-section of the beam and constrained with zero displacements on all surfaces except at the top. The arrangement of the pores for all cases is shown in Figure 7.

All models were subjected to loads of 50, 100, 150, and 200 μN. The deflections were measured at the bottom of the beam at the same distance from the clamp where the load is applied. This reduces errors due to spurious displacements produced by indentation-like behavior at the point of application of the load. A Young's modulus of 219 GPa was used for the UO_2 matrix in all cases so that the effects of porosity could be studied independently from the effects of elastic anisotropy. The results are shown in Table 2.

Table 2: Load-displacement data obtained in Abaqus™ for models with pore clusters located from substrate to the middle and to the end of the beam, the unit for displacement is μm and slope is μN/μm

Model No.	50 μN	100 μN	150 μN	200 μN	Slope	*E* (GPa)	% difference
1	1.89E-02	3.78E-02	5.68E-02	7.57E-02	2640	219	
2	1.99E-02	3.97E-02	5.96E-02	7.94E-02	2520	209	4.5%
3	1.95E-02	3.90E-02	5.85E-02	7.80E-02	2570	213	2.7%
4	1.94E-02	3.89E-02	5.83E-02	7.78E-02	2570	213	2.7%

As expected, the position of pore clusters along the length of the beam plays an important role in the value of Young's modulus from the micro-cantilever experiment, even with the same pore fraction. The largest effect occurs when the pore cluster is close to the substrate, where a reduction of 4.6% on E was obtained comparing to the case with no pores.

In addition to the position of pores along the length of the beam, their position along the height of the cross-section is also likely to play an important role. The classical beam theory clearly indicates that this position will have a strong effect on the moment of inertia, and, through it, on the apparent stiffness of the beam. Rather than performing new FE simulations, beam theory was used to explore this effect by placing a single spherical pore at particular locations along the length of the beam and at different heights on the cross-section. Then, the deflection of the beam was calculated at the point of application of the load, accounting for the variable inertia on the section of the beam where the spherical pore was located. Once the deflection was calculated, equation (1) was used to obtain the apparent Young's modulus

assuming that the inertia was equal to that of the solid cross-section. The pore was placed at distances of L/6, L/2, and 5L/6 from the clamped end, and values of Young's modulus were obtained for three positions along the height (bottom, middle and top). The resulting change in Young's modulus, normalized by the change expected from the rule of mixtures, are shown in Figure 8, which includes an inset showing the different position of the pore on the cross-section used in the calculation.

The results clearly show that the more significant effect can be found for the case when the pore is close to the clamped end and located at the bottom or at the top of the cross-section. These results are in general agreement with the other findings reported above, i.e., that large effects on the deduced value of Young's modulus from the beam deflection can be expected when porosity is close to the substrate. Results also indicate a non-linear relationship between the position of the pore and the deduced Young's modulus, with the effect decreasing sharply with distance from the substrate and for positions close to the centroid of the cross-section. It is noteworthy that the size of the pore chosen (a diameter of one-third of the height of the rectangular part of the cross-section, i.e., dimension b in Table 1) results in a void fraction of 0.4% for the whole beam, so the position of the pore can lead to effects up to 7 times larger than the rule of mixtures, which highlights the importance of the effects of heterogeneity in porosity when the pore size is commensurate with the dimensions of the beam.

In order to produce a more realistic model of the porosity of a microcantilever, the images of the cross-section along the height of beam 5 (Figure 9) were collected with 3D serial sectioning techniques using FIB and EBSD as described earlier. These images were pre-processed first and then imported into the Avizo for microstructural reconstruction. Images were then segmented and labeled (Figure 9b) based on the grain boundaries that could be seen in the images. Then a tetrahedral grid is generated based on the surface mesh. This set contains four models, which can be seen in Figure 10. One of the models is fully solid and the other three contain pores with the same volume fraction.

The only difference among the three models with porosity is that a large pore was located at different places within the beam. Model 1 has about 880,900 elements, whereas models 2 through 4 have approximately 730,000 elements. Model 2 had a large pore at the substrate, whereas models 3 and 4 were created to evaluate the effects of having a large pore in other locations in the microcantilever. A convergence study was conducted, given that the tetrahedral elements used are stiffer than hexahedral elements, and solid elements, in general, can lead to difficulties capturing bending when using coarse meshes. The finished reconstruction is shown in Figure 9b, and the volume of pores is estimated to be 2.5%, which is just half of the expected porosity for the samples used in this study. The discrepancy might be related to the fact that the number of layers obtained from slicing was too low to resolve all the pores present; hence, many pores were neglected during the process, and that the small size of the beams is likely leading to variations in the local volume fraction, particularly given the fact that micro-beams are often machined in regions with low observable porosity, in an effort to reduce the effects of this variable. Figure 9c shows a cross-section view of the reconstructed model, where the internal microstructures (including the pores and various grains) of the model can be clearly observed. The beams were subjected to loads of 50, 100, 150, and 200 μN, and deflections were again measured at the bottom of the beam at the same distance from the clamp where the load is

applied. A Young's modulus of 219 GPa was used for the UO_2 matrix in all cases to separate the effect of porosity from elastic anisotropy. A more detailed analysis on the latter will be reported elsewhere. Results are shown in Table 3.

Table 3: Deflections (in μm) from beam models with different pore cluster locations. The slope is μN/μm.

Model No.	Beam deflection at specific loads Beam Displacement measured at loading location, [μm]				Slope	E (GPa)
	50 μN	100 μN	150 μN	200 μN		
1	1.89E-02	3.78E-02	5.68E-02	7.57E-02	2640	219
2	2.02E-02	4.03E-02	6.04E-02	8.05E-02	2488	207
3	2.07E-02	4.15E-02	6.22E-02	8.29E-02	2410	200
4	2.02E-02	4.04E-02	6.06E-02	8.08E-02	2470	205

From Table 3, it can be seen that although a constant void fraction was kept, the presence of pores along the length of the beam plays an important role in determining the value of apparent Young's modulus deduced from beam deflection. The reduction in Young's modulus ranges from 8.7% for model 3 to 5.4% for model 2. Given the results presented in Table 2 and Figure 8, a larger decrease for the large pore located at the substrate was expected. This is likely a result of the fact that the pore is essentially embedded in the substrate, which is stiffer than the beam, so the reduction in stiffness in the substrate itself is not enough to make a larger difference, particularly given that the large pore is also closer to the middle of the cross-section (see Figure 8). However, the effect can be larger when the pore is in the beam itself, as suggested by the results in Figure 8. Additional information is needed to confirm this interpretation and also to shed light into why the larger decrease is for the case when the pore is located at the middle of the length. Hence, the distribution of normal stresses parallel to the axis of the beam was obtained for all 4 models and results are shown in Figure 11.

The results in Figure 11 indicate that the presence of the larger pores at the substrate and at the end of the beam does not perturb the local stress fields significantly as compared to the case where the beam has no pores. However, the other large pores present in models 2 and 4 can and do change the local stress fields, particularly when they are close to either the top or the bottom of the cross-section. This is consistent with the similarity in the values of apparent Young's modulus for these models. The reduction in Young's modulus for those two cases is likely to stem mostly from the presence of the other pores, particularly given that the large pores are located at the middle of the cross-section. Regarding the model with the pore at the middle of the length (model 3), which has a larger reduction than the other two models, the effect is most likely associated to the fact that the pore orientation was different, leading to a defect with larger effective dimensions in both cross-section area and length in terms of its effects on the moment of inertia. The contour plot in Figure 11c does not show the effect it has on the stresses very well, so stress contours are shown in Figure 12 for a cross-section perpendicular to the axis of the beam that crosses the void at its largest dimension.

The void used in model 3 is large enough to affect the local stress distribution at its lowest point, as shown in Figure 12. This effect is not visible in Figure 11c. In addition, this pore also has a longer dimension along the axis of the beam than for the other two models with pores, increasing the fraction of the beam that has a lower stiffness, leading to a higher overall compliance and hence a lower apparent Young's modulus. The effect in all cases is likely lower than what it could have been if these large pores had been located at either the top or the bottom of the cross-section, as shown in Figure 8.

In taking these idealized results of the effect of the elastic anisotropy and the effect of porosity, microcantilever 5 can be fully analyzed, and the experimental results can be compared with the modeling values. This comparison would be difficult for microcantilevers 1-4 as they were lost during testing, so the internal porosity of the microcantilever was not known. In microcantilever 5 the grains at the substrate have the following orientations and Euler angles. The top grain (pink grain in Figure 9b) is [-1-54] with Euler angles of 60.3, 45, 56.2 degrees. The bottom grain (yellow grain Figure 9b) is [2 5 -4] with Euler angles of 261, 38.5, 34.6 degrees. These values indicate that the top grain would have a Young's modulus of 182 GPa, while the bottom grain would have a Young's modulus of 176 GPa. These values are much higher than the experimentally measured value of 147 GPa shown in Table 1. If porosity calculations and results from Table 3 are applied to this theoretical calculation, it would be expected that the Young's modulus would decrease an average of ~7%. The effect of the porosity would take the 182 GPa value for the top grain to 169 GPa and the 176 GPa value for bottom grain to 163 GPa, which are still larger than the measured value of 147 GPa. However, the porosity was likely underestimated by the coarse serial sectioning used here. Hence, assuming that the pore fraction is closer to the overall 5% measured for the UO_2 sample used and that the effect of the additional porosity leads to a linear increase in its effect on Young's modulus, then, Young's moduli of the grains close to the clamp would decrease to 156 and 151 GPa, a maximum difference of 6% with the experimentally measured value of 147 GPa. Note that assuming a linear effect in this case is conservative and results in Figure 8 and the model presented in [37] indicate that non-linear effects are more likely, suggesting that the agreement could be even better.

The results suggest that creating FE models to account for the actual geometry and location of pores in the region close to the clamp, to about one half of the length of the beam, can lead to more accurate estimations of the actual Young's modulus of the matrix, through tuning the value E used in the simulations and matching the slope of the simulated load-deflection curves to those obtained experimentally. This, however, requires performing serial sectioning with a resolution high enough to resolve all significant pores. It also requires not taking the microcantilevers to fracture to enable the ability to cross section the microcantilever and evaluate its internal porosity distribution. This approach would preclude the measurement of the fracture stress of the microcantilevers, especially in brittle ceramics, where the recovery of the microcantilever after fracture is nearly impossible.

This work also indicates that using microcantilever testing on porous ceramic materials to measure the Young's modulus accurately will be difficult. However, the advent of plasma FIBs and laser systems that allow a large structure to be milled could improve the use of these techniques on porous ceramics. Plasma FIB could allow for the milling of structures an order of magnitude (dozens of microns in width and height) [40] larger than the Ga-FIB based structures

used in this study. While femto-second laser systems would allow even larger structures, approaching two orders of magnitude larger (100s of microns in width and height), which could allow for the average values of the material to be measured [41, 42]. Having this large structure would make it possible for multiple grains to be in the cross section and reduce the effect of porosity. However, a disadvantage of using the larger specimen would be when sub grain properties are being sought as was the initial motivation for this study.

Conclusion

The results and analysis indicate that the presence of pore close to the substrate, will lead to significant reductions in Young's modulus estimation from load-deflection curves made in micro-cantilever beams, where pore size and spacing are of the order of the beam dimensions. These effects are largest for pores close to the clamp due to the larger stresses and strains at those locations. These effects lead to reductions much larger than what can be predicted from models that homogenize the effects of porosity on elastic properties, e.g., rule of mixtures. The effects decrease significantly as pore clusters are moved away from the clamp, for a constant overall pore volume fraction. The results provide insight into steps needed to estimate Young's modulus at small length scales in porous materials using micro-cantilever beam tests and indicate that accounting explicitly for pore geometry and location in FE models is likely necessary to obtain good estimates, but this does not need to be done for the whole length of the beam. It can be seen here with the in-situ loaded beam that when accounting for the porosity in the beam and the elastic anisotropy on the Young's modulus the modeling and experimental values results in the right trend. In addition, the individual Young's modulus of the grains near the substrate needs to be accounted for as it also affects the measured Young's modulus of the microcantilever. Due to the internal porosity of the beam, it could be difficult to evaluate this prior to the testing. Besides, during the ex-situ studies the microcantilever might be lost after fracture and before the cross sectioning can be performed. However, if the elastic modulus of the porous ceramic material is sought such as for spent fuel, a similar approach to the one taken here with the 3D EBSD can be used, provided the serial sectioning is performed at a good enough resolution to resolve the pores well. This would be a time-consuming process but would allow for detailed microstructure and mechanical property information to be extracted from the material. In order to improve the results, samples with mm size grains or in single crystal form could be used to greatly reduce the porosity in the sample and therefore the microcantilever. In addition, this would provide the opportunity to manufacture multiple microcantilevers in the same orientation, allowing the reproducibility of the results to be examined.

Acknowledgments

This work was performed with support from DOE/NE under grant # DE-NE0000670. The assistance of Darrin Byler, Erik Luther and Andrew Nelson at Los Alamos National Laboratory providing UO_2 samples for this work is also greatly appreciated.

References

[1] Y. Rashid, Mathematical modeling and analysis of fuel rods, Nuclear Engineering Design 29(1) (1974) 22-32.

[2] M. Billone, R. Montgomery, Y. Rashid, J. Head, Advancements in the behavioral modeling of fuel elements and related structures, Nuclear engineering design 134(1) (1992) 23-36.
[3] F. Cappia, D. Pizzocri, M. Marchetti, A. Schubert, P. Van Uffelen, L. Luzzi, D. Papaioannou, R. Macian-Juan, V. Rondinella, Microhardness and Young's modulus of high burn-up UO_2 fuel, Journal of Nuclear Materials 479 (2016) 447-454.
[4] J. Spino, J. Cobos-Sabate, F. Rousseau, Room-temperature microindentation behaviour of LWR-fuels, part 1: fuel microhardness, Journal of nuclear materials 322(2-3) (2003) 204-216.
[5] J. Roberts, Y. Ueda, Influence of porosity on deformation and fracture of UO_2, Journal of the American Ceramic Society 55(3) (1972) 117-124.
[6] B. Gong, T. Yao, P. Lei, L. Cai, K.E. Metzger, E.J. Lahoda, F.A. Boylan, A. Mohamad, J. Harp, A.T. Nelson, U_3Si_2 and UO_2 composites densified by spark plasma sintering for accident-tolerant fuels, Journal of Nuclear Materials 534 (2020) 152147.
[7] S. Nichenko, D. Staicu, Thermal conductivity of porous UO_2: Molecular Dynamics study, Journal of Nuclear Materials 454(1-3) (2014) 315-322.
[8] D.E. Armstrong, A.J. Wilkinson, S.G. Roberts, Measuring anisotropy in Young's modulus of copper using microcantilever testing, Journal of materials research 24(11) (2009) 3268-3276.
[9] D. Di Maio, S. Roberts, Measuring fracture toughness of coatings using focused-ion-beam-machined microbeams, Journal of materials research 20(2) (2005) 299-302.
[10] G. Egeland, K. Wheeler, P. Peralta, K. McClellan, S. Maloy, G. Bond, Plastic deformation in zirconium nitride observed by nanoindentation and TEM, Journal of nuclear materials 416(3) (2011) 253-261.
[11] D. Kiener, P. Hosemann, S.A. Maloy, A.M. Minor, In situ nanocompression testing of irradiated copper, Nature materials 10(8) (2011) 608-613.
[12] D. Kiener, A.M. Minor, O. Anderoglu, Y. Wang, S.A. Maloy, P. Hosemann, Application of small-scale testing for investigation of ion-beam-irradiated materials, Journal of Materials Research 27(21) (2012) 2724.
[13] D. Frazer, P. Hosemann, Plasticity of UO_2 studied and quantified via elevated temperature micro compression testing, Journal of Nuclear Materials 525 (2019) 140-144.
[14] B. Gong, D. Frazer, T. Yao, P. Hosemann, M. Tonks, J. Lian, Nano-and micro-indentation testing of sintered UO_2 fuel pellets with controlled microstructure and stoichiometry, Journal of Nuclear Materials 516 (2019) 169-177.
[15] E. Kardoulaki, J.T. White, D.D. Byler, D.M. Frazer, A.P. Shivprasad, T.A. Saleh, B. Gong, T. Yao, J. Lian, K.J. McClellan, Thermophysical and mechanical property assessment of UB2 and UB4 sintered via spark plasma sintering, Journal of Alloys Compounds 818 (2020) 153216.
[16] D. Frazer, D. Jadernas, N. Bolender, J. Madden, J. Giglio, P. Hosemann, Elevated temperature microcantilever testing of fresh U-10Mo fuel, Journal of Nuclear Materials 526 (2019) 151746.
[17] R. Newell, Y. Park, A. Mehta, D. Keiser Jr, Y. Sohn, Mechanical properties examined by nanoindentation for selected phases relevant to the development of monolithic uranium-molybdenum metallic fuels, Journal of Nuclear Materials 487 (2017) 443-452.
[18] M.S. Elbakhshwan, Y. Miao, J.F. Stubbins, B.J. Heuser, Mechanical properties of UO_2 thin films under heavy ion irradiation using nanoindentation and finite element modeling, Journal of Nuclear Materials 479 (2016) 548-558.
[19] K. Kurosaki, Y. Saito, H. Muta, M. Uno, S. Yamanaka, Nanoindentation studies of UO_2 and (U, Ce)O_2, Journal of alloys compounds 381(1-2) (2004) 240-244.

[20] R. Henry, I. Zacharie-Aubrun, T. Blay, N. Tarisien, S. Chalal, X. Iltis, J.-M. Gatt, C. Langlois, S. Meille, Irradiation effects on the fracture properties of UO_2 fuels studied by micro-mechanical testing, Journal of Nuclear Materials 536 (2020) 152179.
[21] R. Henry, I. Zacharie-Aubrun, T. Blay, S. Chalal, J.-M. Gatt, C. Langlois, S. Meille, Fracture properties of an irradiated PWR UO_2 fuel evaluated by micro-cantilever bending tests, Journal of Nuclear Materials 538 (2020) 152209.
[22] K.A. Terrani, M. Balooch, J.R. Burns, Q.B. Smith, Young's modulus evaluation of high burnup structure in UO_2 with nanometer resolution, Journal of Nuclear Materials 508 (2018) 33-39.
[23] F. Cappia, D. Frazer, B.D. Miller, D.J. Murray, A.J. Winston, J.M. Harp, In-situ small-scale mechanical testing of fast reactor mixed oxide pins: completion report, Idaho National Lab.(INL), Idaho Falls, ID (United States), 2019.
[24] H. Stehle, H. Assmann, F. Wunderlich, Uranium dioxide properties for LWR fuel rods, Nuclear engineering design 33(2) (1975) 230-260.
[25] H. Stehle, H. Assman, F. Wunderlich, Uranium Dioxide Properties for LWR Fuel Rods, Nuclear Engineering and Design 33 (1975) 230-260.
[26] A. Doitrand, R. Henry, I. Zacharie-Aubrun, J.-M. Gatt, S. Meille, UO_2 micron scale specimen fracture: Parameter identification and influence of porosities, Theoretical Applied Fracture Mechanics 108 (2020) 102665.
[27] V. Pensée, Q.C. He, Generalized self-consistent estimation of the apparent isotropic elastic moduli and minimum representative volume element size of heterogeneous media, International Journal of Solids and Structures 44(7-8) (2007) 2225-2243.
[28] V. Pensée, Q.-C. He, Generalized self-consistent estimation of the apparent isotropic elastic moduli and minimum representative volume element size of heterogeneous media, International journal of solids structures 44(7-8) (2007) 2225-2243.
[29] M. Abad, S. Parker, D. Frazer, M.R. de Figueiredo, A. Lupinacci, K. Kikuchi, P. Hosemann, Evaluation of the mechanical properties of naturally grown multilayered oxides formed on HCM12A using small scale mechanical testing, Oxidation of Metals 84(1) (2015) 211-231.
[30] D.E.J. Armstrong, A.J. Wilkinson, S.G. Roberts, Measuring anisotropy in Young's modulus of copper using microcantilever testing, Journal of Materials Research 24(11) (2009) 3268-3276.
[31] D.E. Armstrong, E. Tarleton, Bend testing of silicon microcantilevers from 21 C to 770 C, Jom 67(12) (2015) 2914-2920.
[32] B. Comella, M. Scanlon, The determination of the elastic modulus of microcantilever beams using atomic force microscopy, Journal of materials science 35(3) (2000) 567-572.
[33] D. Son, J.-h. Jeong, D. Kwon, Film-thickness considerations in microcantilever-beam test in measuring mechanical properties of metal thin film, Thin solid films 437(1-2) (2003) 182-187.
[34] C. Wilson, A. Ormeggi, M. Narbutovskih, Fracture testing of silicon microcantilever beams, Journal of Applied Physics 79(5) (1996) 2386-2393.
[35] J. Gong, A. Wilkinson, Investigation of elastic properties of single-crystal α-Ti using microcantilever beams, Philosophical magazine letters 90(7) (2010) 503-512.
[36] C. Hsu, C. Tsou, W. Fang, Measuring thin film elastic modulus using a micromachined cantilever bending test by nanoindenter, Journal of Micro/Nanolithography, MEMS, and MOEMS 6(3) (2007) 033011.
[37] N. Igata, K. Domoto, Fracture stress and elastic modulus of uranium dioxide including excess oxygen, Journal of Nuclear Materials 45(4) (1973) 317-322.

[38] N. Igata, K. Domoto, Fracture stress and elastic modulus of uranium dioxide including excess oxygen, J. Nuc. Mat. 45 (1973) 317-322.
[39] J.F. Nye, Physical properties of crystals: their representation by tensors and matrices, Oxford university press1985.
[40] Y. Xiao, J. Wehrs, H. Ma, T. Al-Samman, S. Korte-Kerzel, M. Göken, J. Michler, R. Spolenak, J.M. Wheeler, Investigation of the deformation behavior of aluminum micropillars produced by focused ion beam machining using Ga and Xe ions, Scripta Materialia 127 (2017) 191-194.
[41] M.J. Pfeifenberger, M. Mangang, S. Wurster, J. Reiser, A. Hohenwarter, W. Pfleging, D. Kiener, R. Pippan, The use of femtosecond laser ablation as a novel tool for rapid micro-mechanical sample preparation, Materials Design 121 (2017) 109-118.
[42] Q. McCulloch, J.G. Gigax, P. Hosemann, Femtosecond Laser Ablation for Mesoscale Specimen Evaluation, Jom 72(4) (2020) 1694-1702.

Captions

Figure 1: Image showing a typical micro-cantilever beam in the test.

Figure 2: (a) A typical load-displacement curve from an in-situ SEM test of a microcantilever, (b) A SEM image of the microcantilever beam prior to testing. This cantilever was not loaded to fracture, (c) A representative load-displacement curve from an ex-situ test where the microcantilever was fractured. The plot is the raw data from the MicroMaterials nanoindentation system that would not account for potential penetration of the Berkovich tip into the microcantilever, and (d) Scans of the microcantilever Before and after testing obtained using the scanning feature of the MicroMaterials indenter.

Figure 3: (a) A visual representation of the model of a non-porous microcantilever, and (b) A schematic of the micro-cantilever showing the dimensions.

Figure 4: Orientation map (top view) of different grains in the beam. The color of the grains corresponds to their crystallographic orientation perpendicular to the image as per the standard triangle legend.

Figure 5: Schematic graph showing the assumed ‘bamboo structure’ for polycrystalline beams. Included in the figure is L_i and L_{i-1} for grain 2 in the “bamboo structure” cantilever.

Figure 6: Plots of effective Young’s modulus versus the length fraction r when the beam has 2 grains with different Young’s moduli. (a) When the grain with higher Young’s modulus (334 GPa) is close to the substrate, and (b) when the grain with lower Young’s modulus (164 GPa) is close to the substrate.

Figure 7: Models with pores concentrated at different parts of the beam: (a) solid beam with no pores (model 1), (b) beam with pores close to the substrate (model 2), (c) beam with pores in the middle part (model 3), (d) beam with pores close to the free end (model 4).

Figure 8: Normalized change in apparent Young's modulus as a result of the presence of a single pore as a function of its position in the beam.

Figure 9: (a) Raw images collected using FIB at UCB, (b) Reconstructed 3D model with Avizo using EBSD images, and (c) the cross-section view of the reconstructed model showing the internal microstructures of the beam.

Figure 10: Models with pores located at different parts of the beam with the largest pore in the microcantilever highlighted with the yellow circle: (a) solid beam with no pores (model 1), (b) beam with the big pore close to the substrate (model 2) which is most representative of the beam used, (c) beam with the big pore in the middle part (model 3), (d) beam with the big pore close to the free end (model 4).

Figure 11: Normal stresses along the axis of the beam. (a) Beam with no pores (model 1 in Table 3), (b) Beam with pores and a large pore in the substrate (model 2 in Table 3), (c) Beam with pores and a large pore in the middle of the length (model 3 in Table 3), and (d) Beam with pores and a large pore towards the end of the length (model 4 in Table 3). The legend and coordinate axes in (a) apply to all figures.

Figure 12: Normal stresses along the axis of the beam on a cross-section perpendicular to the x axis. The legend in Figure 11a also apply in this case.

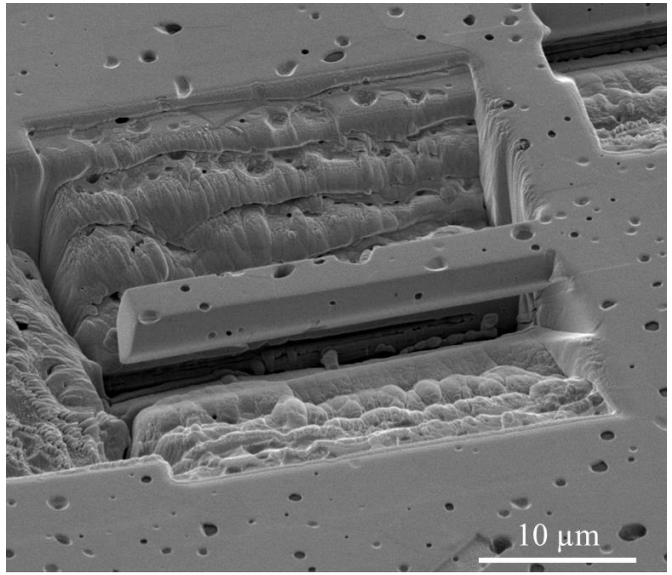

Figure 1: Image showing a typical micro-cantilever beam in the test.

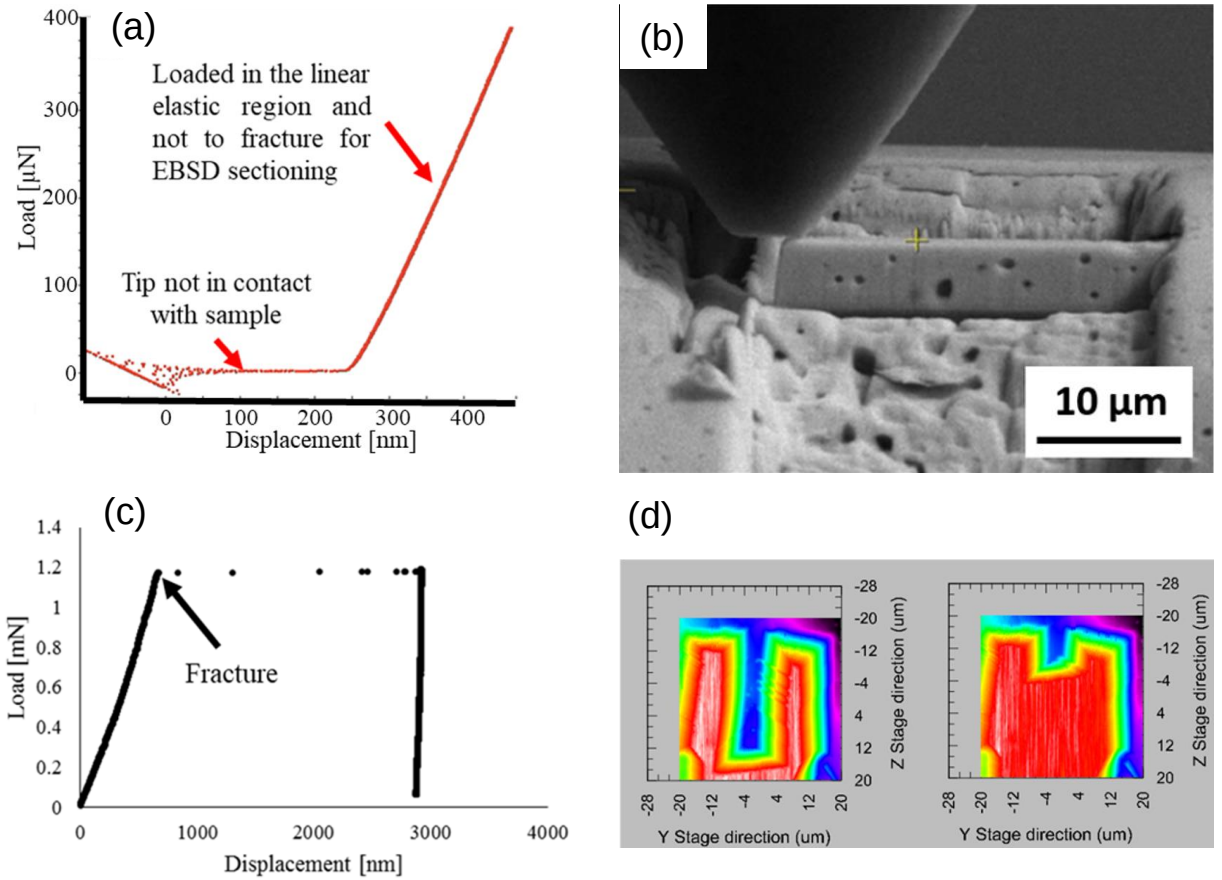

Figure 2: (a) A typical load-displacement curve from an in-situ SEM test of a microcantilever, (b) A SEM image of the microcantilever beam prior to testing. This cantilever was not loaded to fracture, (c) A representative load-displacement curve from an ex-situ test where the microcantilever was fractured. The plot is the raw data from the MicroMaterials nanoindentation system that would not account for potential penetration of the Berkovich tip into the microcantilever, and (d) Scans of the microcantilever Before and after testing obtained using the scanning feature of the MicroMaterials indenter.

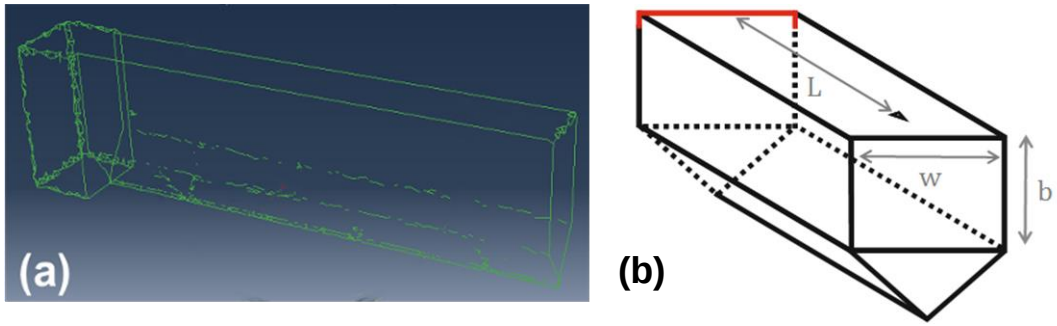

Figure 3: (a) A visual representation of the model of a non-porous microcantilever. (b) A schematic of the micro-cantilever showing the dimensions.

Figure 4: Orientation map (top view) of different grains in the beam. The color of the grains corresponds to their crystallographic orientation perpendicular to the image as per the standard triangle legend.

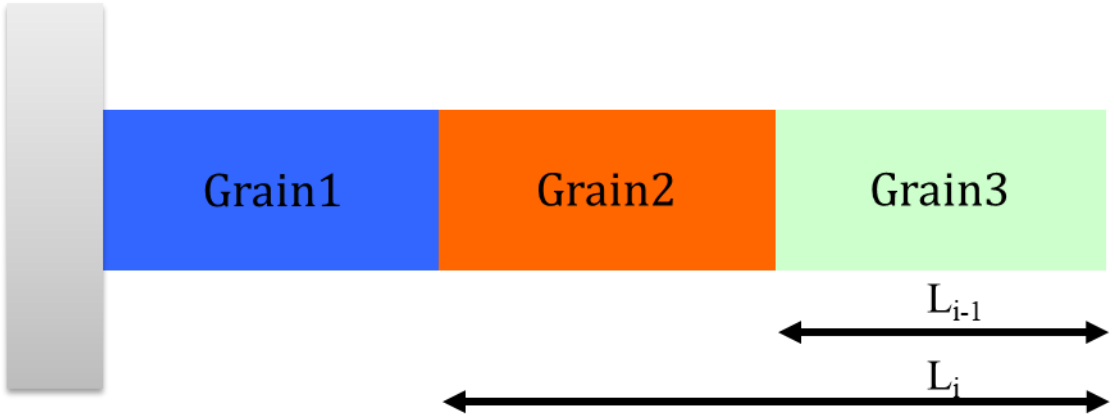

Figure 5: Schematic graph showing the assumed ‘bamboo structure’ for polycrystalline beams. Included in the figure is L_i and L_{i-1} for grain 2 in the “bamboo structure” cantilever.

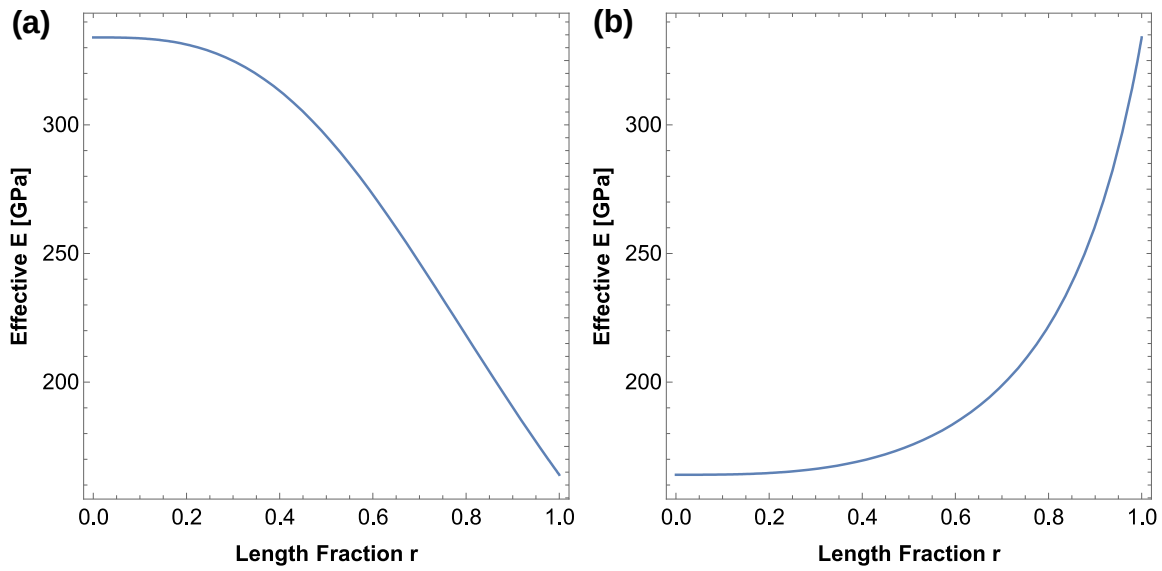

Figure 6: Plots of effective Young's modulus versus the length fraction r when the beam has 2 grains with different Young's moduli. (a) When the grain with higher Young's modulus (334 GPa) is close to the substrate, and (b) when the grain with lower Young's modulus (164 GPa) is close to the substrate.

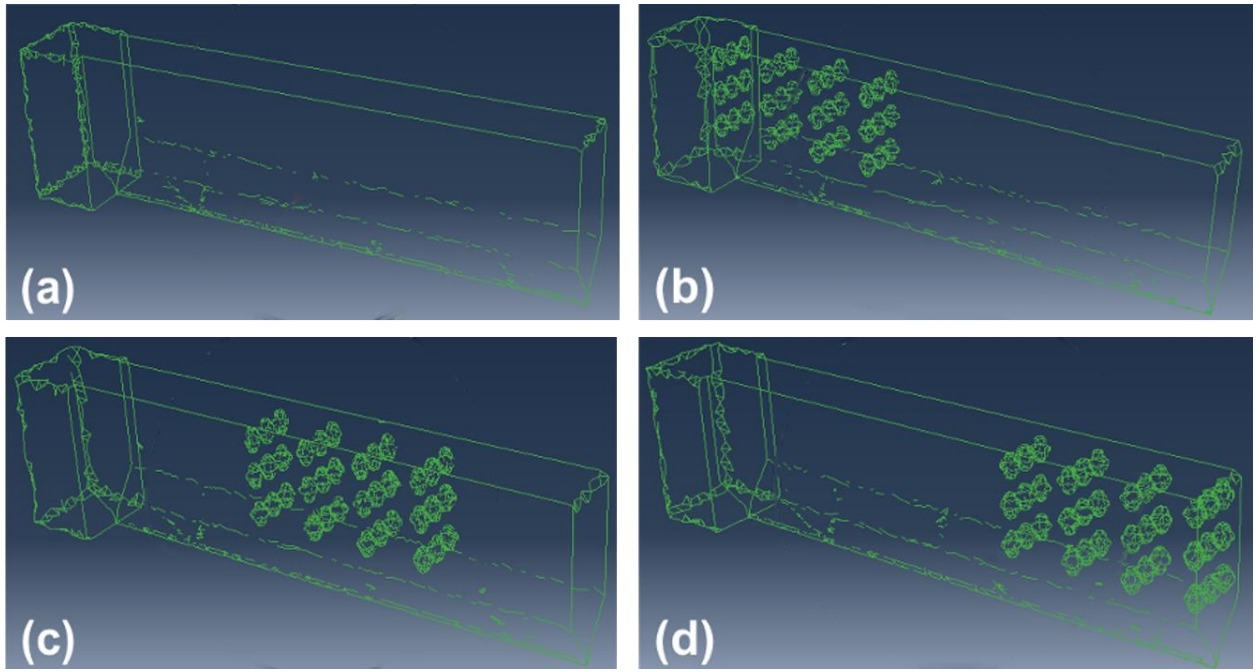

Figure 7: Models with pores concentrated at different parts of the beam: (a) solid beam with no pores (model 1); (b) beam with pores close to the substrate (model 2); (c) beam with pores in the middle part (model 3); (d) beam with pores close to the free end (model 4).

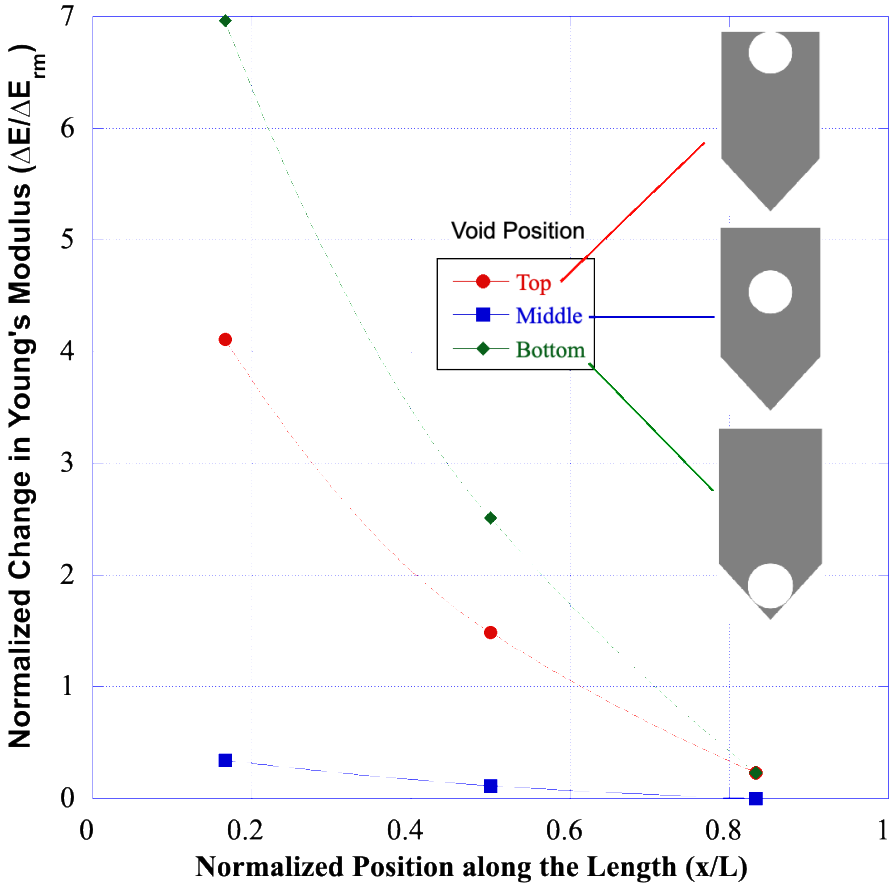

Figure 8: Normalized change in apparent Young's modulus as a result of the presence of a single pore as a function of its position in the beam.

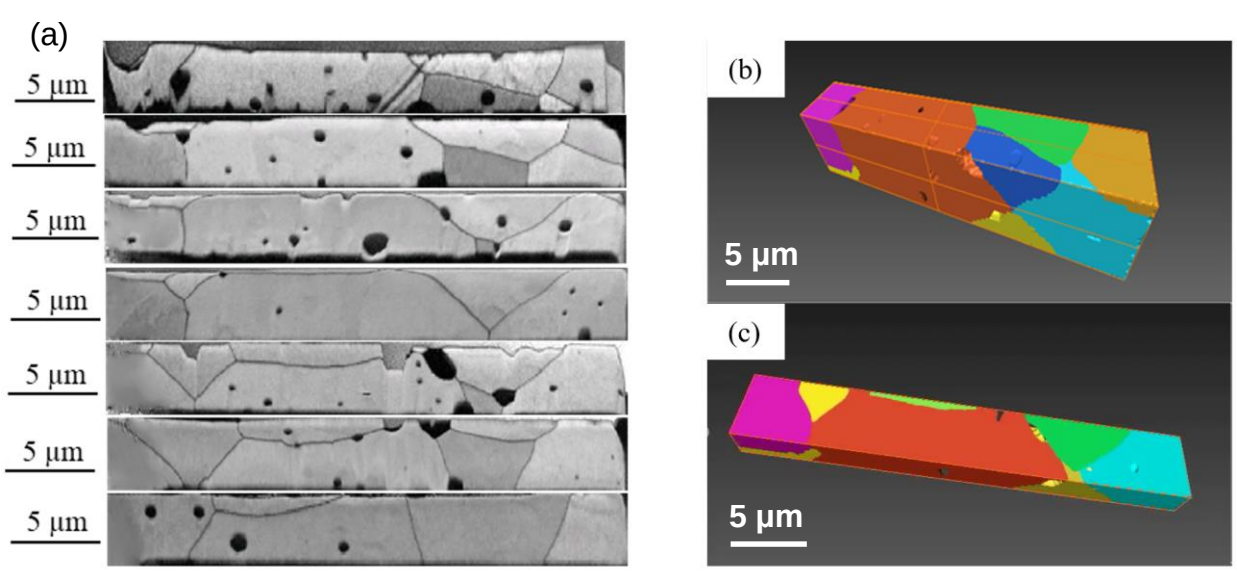

Figure 9: (a) Raw images collected using FIB at UCB; (b) Reconstructed 3D model with Avizo using EBSD images; and (c) the cross-section view of the reconstructed model showing the internal microstructures of the beam.

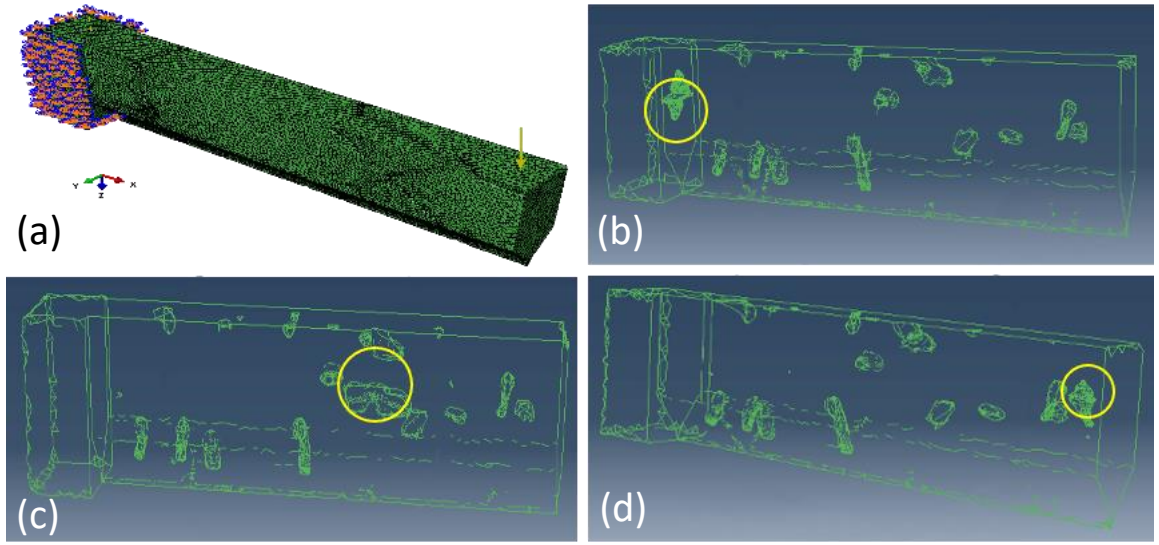

Figure 10: Models with pores located at different parts of the beam with the largest pore in the microcantilever highlighted with the yellow circle: (a) solid beam with no pores (model 1); (b) beam with the big pore close to the substrate (model 2) which is most representative of the beam used; (c) beam with the big pore in the middle part (model 3); (d) beam with the big pore close to the free end (model 4).

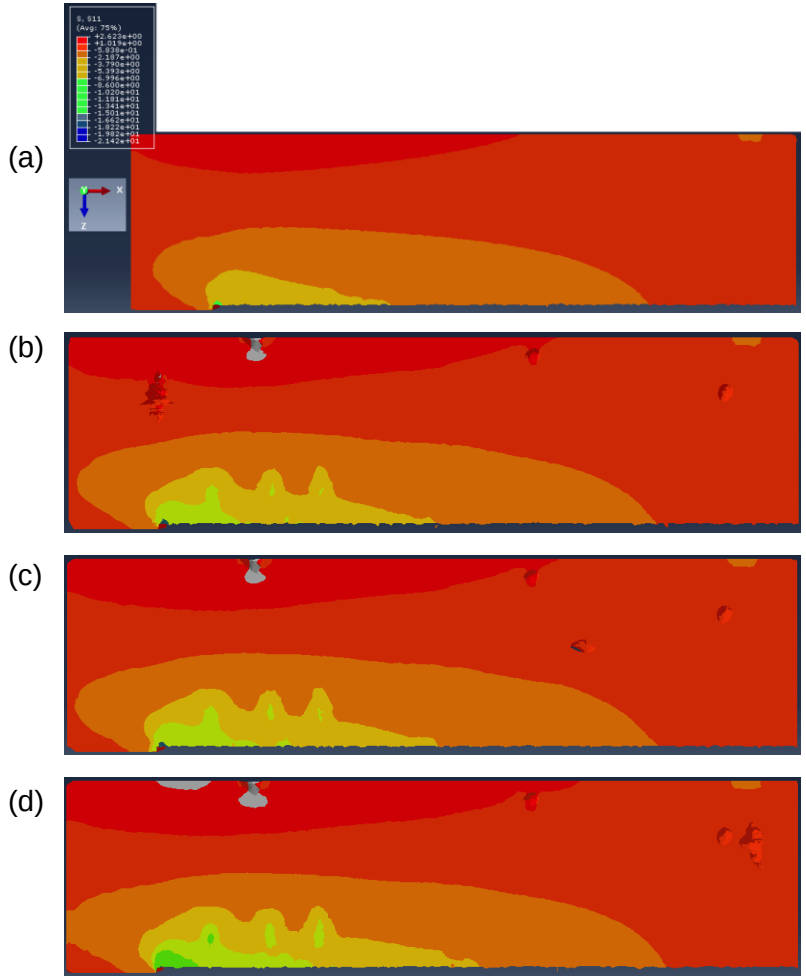

Figure 11: Normal stresses along the axis of the beam. (a) Beam with no pores (model 1 in Table 3). (b) Beam with pores and a large pore in the substrate (model 2 in Table 3). (c) Beam with pores and a large pore in the middle of the length (model 3 in Table 3). (d) Beam with pores and a large pore towards the end of the length (model 4 in Table 3). The legend and coordinate axes in (a) apply to all figures.

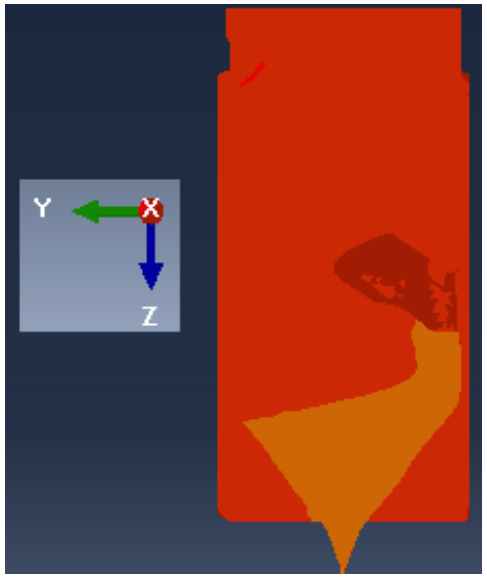

Figure 12: Normal stresses along the axis of the beam on a cross-section perpendicular to the x axis. The legend in Figure 11a also apply in this case.